

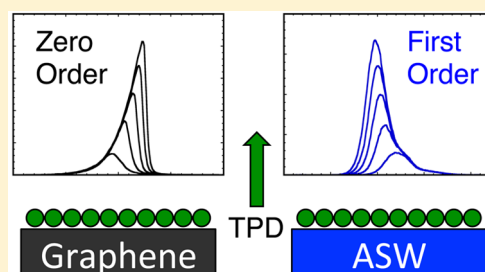
# Desorption Kinetics of Ar, Kr, Xe, N<sub>2</sub>, O<sub>2</sub>, CO, Methane, Ethane, and Propane from Graphene and Amorphous Solid Water Surfaces

R. Scott Smith,\* R. Alan May, and Bruce D. Kay\*

Physical and Computational Sciences Directorate, Pacific Northwest National Laboratory, Richland, Washington 99352, United States

**S** Supporting Information

**ABSTRACT:** The desorption kinetics for Ar, Kr, Xe, N<sub>2</sub>, O<sub>2</sub>, CO, methane, ethane, and propane from graphene-covered Pt(111) and amorphous solid water (ASW) surfaces are investigated using temperature-programmed desorption (TPD). The TPD spectra for all of the adsorbates from graphene have well-resolved first, second, third, and multilayer desorption peaks. The alignment of the leading edges is consistent with the zero-order desorption for all of the adsorbates. An Arrhenius analysis is used to obtain desorption energies and prefactors for desorption from graphene for all of the adsorbates. In contrast, the leading desorption edges for the adsorbates from ASW do not align (for coverages < 2 ML). The nonalignment of TPD leading edges suggests that there are multiple desorption binding sites on the ASW surface. Inversion analysis is used to obtain the coverage dependent desorption energies and prefactors for desorption from ASW for all of the adsorbates.



## I. INTRODUCTION

The desorption kinetics for a wide range of molecules are needed to develop models to determine the present and historical composition of astrophysical bodies such as comets, interplanetary ices, interplanetary dust, and planetary surfaces.<sup>1–9</sup> These bodies often consist of carbonaceous materials and/or have deposits of amorphous solid water (ASW).<sup>6,9</sup> While not identical to astrophysical conditions, laboratory-based desorption measurements are currently used to provide this data. Researchers have used amorphous carbon or highly oriented pyrolytic graphite (HOPG) as analogs for carbonaceous surfaces.<sup>6,9–12</sup> Similarly, ASW analogous can be created in the laboratory by depositing water vapor onto a low temperature substrate (typically < 130 K).<sup>13–30</sup> Determining the desorption mechanism (order) is important, as it will affect the overall desorption rate in any model used to describe the behavior of astrophysical ices.<sup>3–9</sup>

In a recent paper we reported on the desorption of three astrophysically relevant molecules, methanol, ethanol, and water, from a layer of graphene grown on Pt(111).<sup>31</sup> For methanol and ethanol, desorption from the first, second, third, and multilayer is consistent with a zero-order desorption mechanism. For water, the desorption of thin films (<10 layers) is complicated by dewetting that occurs on the hydrophobic graphene surface, but for thicker water films (>10 layers) zero-desorption kinetics are observed. The observation of zero-order desorption kinetics is in contrast to the fractional-order desorption kinetics reported for the same three molecules on HOPG (graphite).<sup>7,9,32–34</sup>

In this paper we study the desorption kinetics of Ar, Kr, Xe, N<sub>2</sub>, O<sub>2</sub>, CO, methane, ethane, and propane from two astrophysically relevant substrates, graphene and ASW. Molecular beam dosing and temperature-programmed desorp-

tion (TPD) are used to measure the desorption kinetics for each adsorbate from both surfaces. Well-resolved first, second, third, and multilayer desorption peaks are observed for all of the adsorbates desorbing from the graphene substrate. The alignment of the TPD leading edges is consistent with zero-order desorption kinetics. In contrast, the desorption of the same adsorbates (for coverages < 2 ML) from ASW are markedly nonzero order. The observed desorption behavior from ASW suggests that there are multiple desorption binding sites on the ASW surface. An Arrhenius analysis is used to obtain desorption energies and prefactors for desorption from graphene and inversion analysis is used to obtain the coverage dependent desorption energies and the prefactors for desorption from ASW. The contrasting desorption mechanisms from these two substrates is an important consideration for kinetic models for adsorbate desorption from astrophysical bodies.

## II. EXPERIMENTAL SECTION

The experiments were performed in an ultrahigh vacuum system (UHV) with a base pressure of <1 × 10<sup>-10</sup> Torr. A detailed description of the chamber and approach has been published previously and only a brief summary will be given here.<sup>23,35</sup> A Pt(111) single crystal (~1 cm diameter) was used as a substrate to grow the graphene layer and ASW films. The Pt(111) was cleaned using a procedure of Ne<sup>+</sup> sputtering (1.5 keV), oxygen exposure, and temperature annealing (1100 K). The substrate was cooled by a closed cycle helium cryostat to a

**Special Issue:** Bruce C. Garrett Festschrift

**Received:** October 13, 2015

**Revised:** November 17, 2015

**Published:** November 23, 2015



base temperature of  $\sim 25$  K. The sample was heated resistively through two tantalum leads spot-welded to the back of the Pt(111) crystal. The temperature was measured with a K-type thermocouple spot-welded to the back of the Pt(111) sample. The temperature was measured with a precision of better than  $\pm 0.01$  K and was calibrated to an absolute accuracy of better than  $\pm 2$  K utilizing the desorption of Kr and H<sub>2</sub>O multilayers.

The graphene layer was grown by heating the Pt(111) substrate to 1100 K and exposing it to a molecular beam of decane. Prior work has shown that this procedure produces a well-ordered, single layer of carbon with the structure of graphite.<sup>36,37</sup> The ASW films were grown using a quasi-effusive molecular beam that was collimated by three stages of differential pumping before impinging on the substrate at normal incidence at 60 K. This deposition temperature was chosen to eliminate the ASW microporosity that can develop at lower temperature deposition.<sup>23</sup> The water beam had a flux of 0.87 ML/s (water) and a beam diameter slightly larger than that of the Pt(111) substrate. A water monolayer (1 ML) is defined as the monolayer saturation coverage on the Pt(111) substrate and corresponds to  $\sim 1.1 \times 10^{15}$  molecules/cm<sup>2</sup>. All adsorbates were deposited at normal incidence at 25 K using a separate quasi-effusive molecular beam collimated by four stages of differential pumping. A ML for each adsorbate was defined by the dose needed to saturate the monolayer desorption peak on graphene. Desorption spectra were obtained with an Extrel quadrupole mass spectrometer were in a line-of-sight configuration. The mass spectrometer signal was converted to ML/s using the ML definition. A linear heating rate of 1 K/s was used for all of the TPD experiments.

### III. RESULTS AND DISCUSSION

**A. Desorption Kinetics from Graphene.** Figure 1 displays TPD spectra for methane films deposited at 25 K on graphene and heated at 1.0 K/s. The top panel, Figure 1a, displays desorption spectra with coverages from 0.1 to 1.0 ML (blue curves), 1.2 to 2.0 ML (red curves), and 2.2 to 3.0 ML (black curves). The spectra show that the desorption from the first, second, and third layers are clearly resolved and that the leading edges on all three peaks are aligned. This alignment is a signature of zero-order desorption kinetics. For submonolayer coverages, zero-order desorption is surprising but can be explained by the formation of a two-dimensional equilibrium between individual adsorbates (gas phase) and islands (condensed phase).<sup>38</sup> The chemical potential and thus the vapor pressure of the system are defined by this two-dimensional, two-phase coexistence. If this equilibrium is maintained during the desorption process (i.e., surface diffusion is fast compared to desorption rate) then the vapor pressure (i.e., the desorption rate) depends only on temperature and not on coverage. The result is the alignment of the desorption leading edges and zero-order desorption kinetics. This follows naturally from the Gibb's phase rule.

The spectra in Figure 1a also show a plateau region between the first and second layer desorption peaks (between  $\sim 40$  and  $\sim 52$  K). When plotted on a linear scale the desorption rate in the plateau region appears to be close to zero (a baseline). However, when the spectra are plotted on a log scale, as in Figure 1b, it is clear that the desorption rate is not zero. Desorption in this region is attributed to desorption from a compressed monolayer and this phenomenon has been described in detail before.<sup>39</sup> Simply put, there is an energetic advantage for a molecule to be in direct contact with the

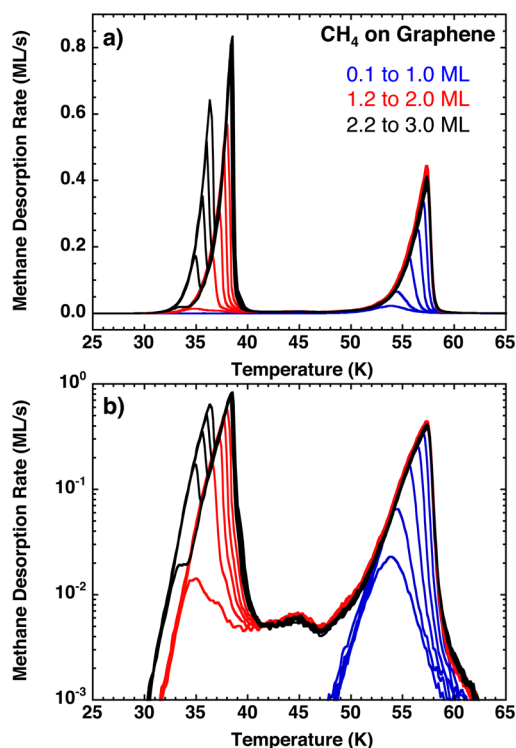


**Figure 1.** (a) TPD spectra for methane films deposited at 25 K on graphene and heated at 1.0 K/s for coverages from 0.1 to 1.0 ML (blue curves), 1.2 to 2.0 ML (red curves), and 2.2 to 3.0 ML (black curves). (b) A log plot of the TPD spectra displayed in (a).

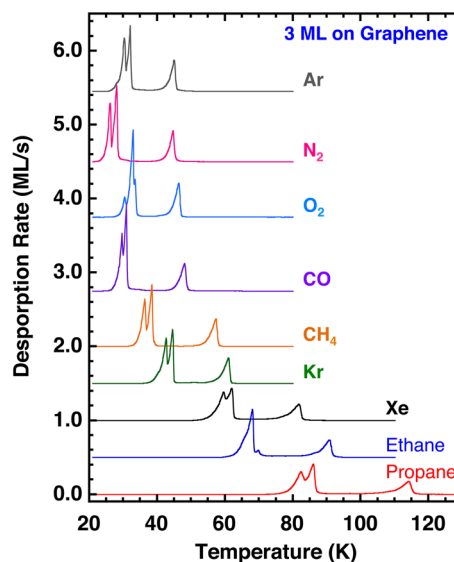


**Figure 2.** 3 ML TPD spectra for Ar, N<sub>2</sub>, O<sub>2</sub>, CO, CH<sub>4</sub>, Kr, Xe, ethane, and propane deposited on graphene. All adsorbates were deposited at 25 K and heated at 1.0 K/s. The spectra are offset vertically for clarity of display.

substrate despite the energetic penalty that results from the repulsion of “squeezing” into the first layer. Eventually the energy penalty for compressing into the first layer outweighs the benefit and molecules begin to adsorb into the second layer.

The analogous filling curve experiments were conducted for Ar, Kr, Xe, N<sub>2</sub>, O<sub>2</sub>, CO, ethane, and propane deposited at 25 K on graphene and heated at 1.0 K/s (not shown). The same alignment of the desorption leading edges was observed in all

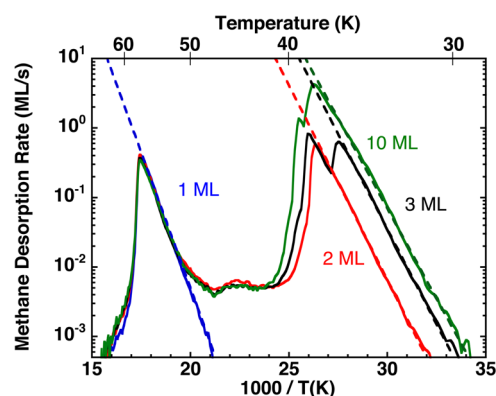


**Figure 3.** Arrhenius plot of the TPD spectra of methane on graphene (solid lines) with coverages of 1 (blue), 2 (red), 3 (black), and 10 ML (green). The corresponding dashed lines are Arrhenius fits and the parameters are given in Table 1.

cases. Figure 2 displays the 3 ML TPD spectra for all of the adsorbates. All of the spectra have well-resolved first and second layer desorption peaks with a plateau desorption (compression) region in between. A third layer desorption feature is also apparent in the spectra but the degree of separation from the second layer peak varies among the adsorbates. These results show that all of the adsorbates desorb in a layer-by-layer fashion and this, combined with the alignment of the leading edges observed in the filling curve experiments (not shown), confirm a zero-order desorption mechanism.

An Arrhenius function,  $\text{rate} = \nu \exp(-E_{\text{des}}/RT)$ , where  $\nu$  is the prefactor and  $E_{\text{des}}$  is the desorption activation energy was used to determine the desorption energies. Figure 3 is an Arrhenius plot of the TPD spectra from Figure 1 with coverages of 1 (blue), 2 (red), 3 (black), and 10 ML (green) of methane. The dashed lines are Arrhenius fits to the leading edges of each desorption peak. There is excellent agreement between the experiment and Arrhenius fit. The same analysis

**Table 1.** Arrhenius Desorption Parameters from Graphene

adsorbate	layer	arrhenius parameters <sup>a</sup>		$\Delta H_{\text{sub}}$ (kJ/mol)	$\Delta H_{\text{sub}}$ source
		$\nu$ (ML/s)	$E_a$ (kJ/mol)		
argon (Ar)	first	$1.6 \times 10^{12}$	10.8		
	second	$1.4 \times 10^{13}$	8.1		
	third	$1.6 \times 10^{13}$	7.7		
	multilayer	$1.1 \times 10^{13}$	7.5	7.7	ref 41 ( $\Delta H_{\text{fus}} + \Delta H_{\text{vap}}$ )
krypton (Kr)	first	$2.8 \times 10^{12}$	15.1		
	second	$1.1 \times 10^{13}$	11.2		
	third	$6.7 \times 10^{12}$	10.6		
	multilayer	$6.0 \times 10^{13}$	11.2	10.7	ref 41 ( $\Delta H_{\text{fus}} + \Delta H_{\text{vap}}$ )
xenon (Xe)	first	$6.0 \times 10^{10}$	17.8		
	second	$3.6 \times 10^{10}$	12.9		
	third	$2.0 \times 10^{11}$	13.3		
	multilayer	$4.7 \times 10^{12}$	14.6	14.9	ref 41 ( $\Delta H_{\text{fus}} + \Delta H_{\text{vap}}$ )
nitrogen (N <sub>2</sub> )	first	$1.7 \times 10^{13}$	11.6		
	second	$3.1 \times 10^{13}$	7.2		
	third	$8.3 \times 10^{12}$	6.5		
	multilayer	$4.3 \times 10^{14}$	7.2	6.3	ref 41 ( $\Delta H_{\text{fus}} + \Delta H_{\text{vap}}$ )
carbon monoxide (CO)	first	$1.9 \times 10^{13}$	12.5		
	second	$6.3 \times 10^{14}$	8.7		
	third	$2.2 \times 10^{13}$	7.6		
	multilayer	$4.1 \times 10^{13}$	7.6	6.9	ref 41 ( $\Delta H_{\text{fus}} + \Delta H_{\text{vap}}$ )
oxygen (O <sub>2</sub> )	first	$1.1 \times 10^{13}$	11.8		
	second	$7.2 \times 10^{14}$	9.3		
	third	$1.3 \times 10^{14}$	8.6		
	multilayer	$3.2 \times 10^{14}$	8.6	7.3	ref 41 ( $\Delta H_{\text{fus}} + \Delta H_{\text{vap}}$ )
methane (CH <sub>4</sub> )	first	$2.1 \times 10^{13}$	14.9		
	second	$4.2 \times 10^{14}$	10.7		
	third	$9.5 \times 10^{14}$	10.5		
	multilayer	$2.5 \times 10^{14}$	9.9	9.2	ref 40
ethane (C <sub>2</sub> H <sub>6</sub> )	first	$4.6 \times 10^{13}$	24.8		
	second	$2.2 \times 10^{16}$	21.5		
	third	$1.2 \times 10^{16}$	20.9		
	multilayer	$3.7 \times 10^{16}$	21.4	20.5	ref 40
propane (C <sub>3</sub> H <sub>8</sub> )	first	$3.8 \times 10^{13}$	31.2		
	second	$4.0 \times 10^{14}$	24.7		
	third	$1.7 \times 10^{16}$	26.3		
	multilayer	$6.0 \times 10^{17}$	28.5	28.5	ref 40

<sup>a</sup>Due to compensation effects, equally good fits can be obtained for a range of any individual Arrhenius fit parameter. To estimate the individual parameter error, one parameter was held fixed and other was varied. Typical errors were a factor of 2 for  $\nu$  and  $\pm 5\%$  for  $E_a$ .

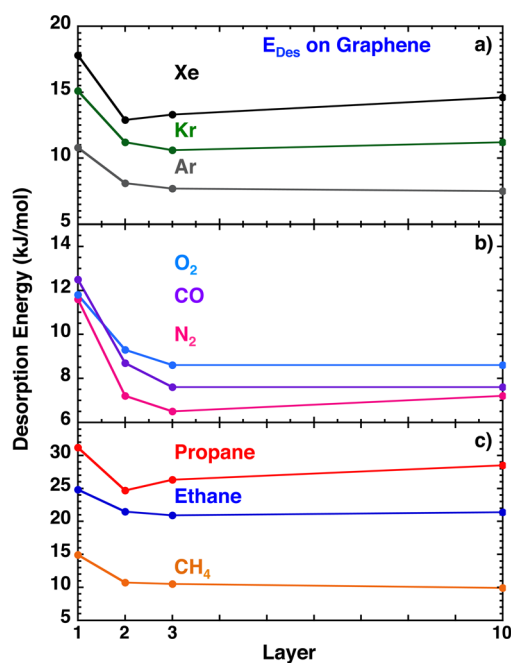


**Figure 4.** Plot of the desorption energy ( $E_{\text{des}}$ ) on graphene vs the desorption layer for (a) Xe, Kr, and Ar, (b)  $\text{O}_2$ ,  $\text{N}_2$ , and CO, and (c) methane, ethane, and propane. The numerical values are given in Table 1.

was used to analyze the first, second, third, and multilayer desorption peaks for the other eight adsorbates (not shown). The fit parameters are summarized in Table 1. Because of compensation effects between the two parameters, fits of similar quality can be obtained for a range of prefactors and activation energies. An estimate of the error was obtained by holding one parameter constant and letting the other parameter vary to fit the data. Based on this procedure we estimate an error of a factor of 2 for  $\nu$  and  $\pm 5\%$  for  $E_{\text{des}}$ . In some cases, the third layer desorption peak is not well-resolved from the multilayer peak and for this reason the  $E_{\text{des}}$  error for this layer may be slightly more.

Figure 4 displays a plot of the desorption energy versus layer (first, second, third, and tenth) for all of the adsorbates. The atomic adsorbates (Ar, Kr, and Xe) are plotted in Figure 4a, the diatomic species ( $\text{O}_2$ ,  $\text{N}_2$ , and CO) are plotted in Figure 4b, and the molecular species (methane, ethane, and propane) are plotted in Figure 4c. In all cases, the first layer desorption energy is the largest, and in general, there is only a small difference between the desorption energies for the third and tenth layers. One would expect that the desorption energy for thicker layers would approach sublimation energy. The sublimation energies are given in Table 1.<sup>40,41</sup> The desorption energies from the tenth layer are typically slightly higher than the sublimation energy and the values for most of the adsorbates are within  $\sim 5\%$  of its value. The exception is the diatomics ( $\text{N}_2$ ,  $\text{O}_2$ , and CO) whose  $E_{\text{des}}$  values are 10–20% greater than their respective sublimation energies.

**B. Desorption Kinetics from ASW.** The TPD spectra for Ar, Kr, Xe,  $\text{N}_2$ ,  $\text{O}_2$ , CO, methane, ethane, and propane from ASW films were also obtained. In these experiments 100 ML thick ASW films were deposited at normal incidence on a graphene covered Pt(111) surface at 60 K. The adsorbates were subsequently deposited at normal incidence at 25 K. The TPD spectra for Ar, Kr, and Xe are displayed in Figure 5, the spectra

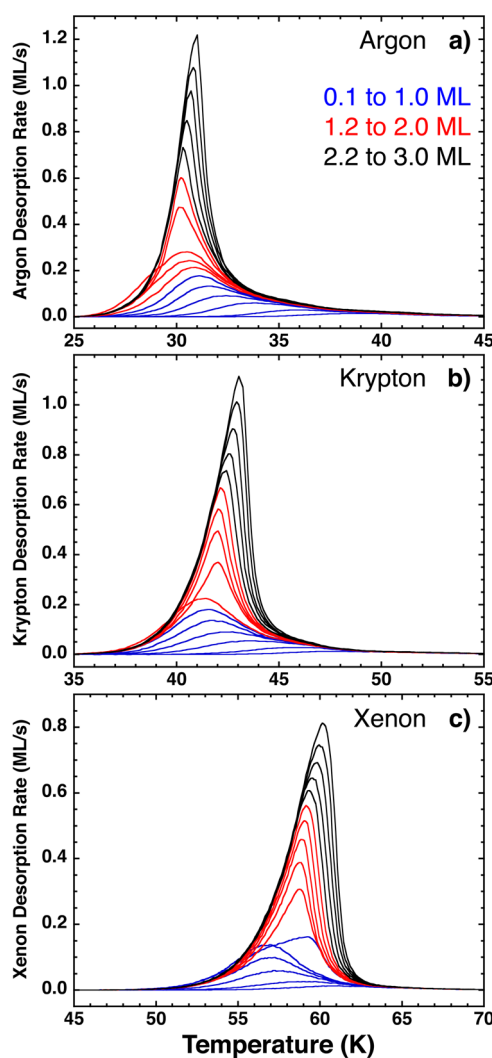


**Figure 5.** TPD spectra for (a) argon, (b) krypton, and (c) xenon on ASW for coverages from 0.1 to 1.0 ML (blue curves), 1.2 to 2.0 ML (red curves), and 2.2 to 3.0 ML (black curves). All adsorbates were deposited at 25 K and heated at 1.0 K/s.

for  $\text{O}_2$ ,  $\text{N}_2$ , and CO are displayed in Figure 6, and the spectra for methane, ethane, and propane are displayed in Figure 7. In all of the figures, the spectra with coverages from 0.1 to 1.0 ML are shown as blue curves, coverages from 1.2 to 2.0 ML are shown as red curves, and coverages from 2.2 to 3.0 ML are shown as black curves. There are some qualitative features exhibited by all of the adsorbates. First, for all of the adsorbates the submonolayer coverage spectra (blue curves) do not align on the leading desorption edge. Second, in most cases there is no clear resolution between the first and second layer desorption peaks. Instead there is a continuous evolution of the desorption leading edge until alignment occurs at higher coverages. For the atomic adsorbates (Ar, Kr, and Xe) in Figure 5, the TPD leading edges begin to align when the coverage is between 1 and 2 ML. For the diatomic species ( $\text{O}_2$ ,  $\text{N}_2$ , and CO) in Figure 6 and the molecular species in Figure 7, the TPD leading edges begin to align when the coverage is between 2 and 3 ML. Finally, the trailing edges of submonolayer TPD spectra are aligned. This behavior suggests a distribution of binding site energies and that the adsorbates have sufficient mobility prior to desorption to find the highest energy binding sites.

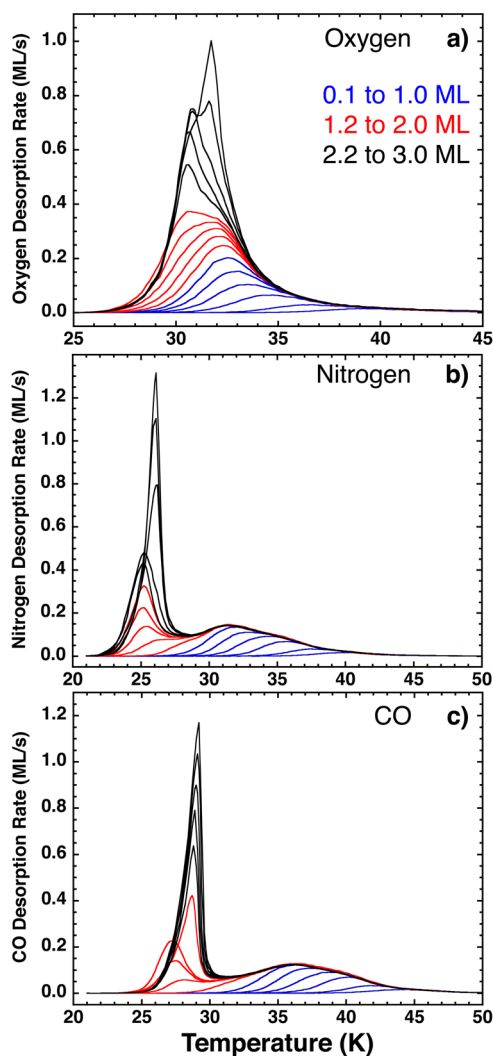


**Figure 6.** TPD spectra for (a) oxygen, (b) nitrogen, and (c) CO on ASW for coverages from 0.1 to 1.0 ML (blue curves), 1.2 to 2.0 ML (red curves), and 2.2 to 3.0 ML (black curves). All adsorbates were deposited at 25 K and heated at 1.0 K/s.

These results are in sharp contrast to the desorption results observed for the same adsorbates on graphene. The monolayer TPD peaks on ASW occur at markedly lower temperatures than they do on graphene. This clearly indicates that the interaction of the adsorbates with ASW is noticeably weaker than their interaction with graphene. The relatively simple Arrhenius analysis used to obtain the binding energies on graphene (Table 1) will not work here. In the next section we describe the inversion analysis method to extract the coverage dependent adsorbate desorption energies from ASW.

**C. Inversion Analysis of Desorption from ASW.** The behavior of the submonolayer TPD spectra in Figures 5, 6, and 7 are consistent with desorption from a surface with a distribution of adsorbate binding sites and energies. In such cases, an “inversion” method can be used to determine the coverage dependent adsorbate binding energies. The procedure has been described in detail elsewhere.<sup>23,42–46</sup> Briefly, the adsorbate desorption rate is given by the Polanyi–Wigner rate equation,  $d\theta/dt = -\nu\theta^n \exp(-E_{\text{des}}/RT)$ , where  $\theta$  is the coverage,  $T$  is the temperature,  $E$  is the desorption activation energy,  $R$  is the gas constant,  $\nu$  is the prefactor, and  $n$  is the desorption order. One assumes that  $\nu$  is coverage independent

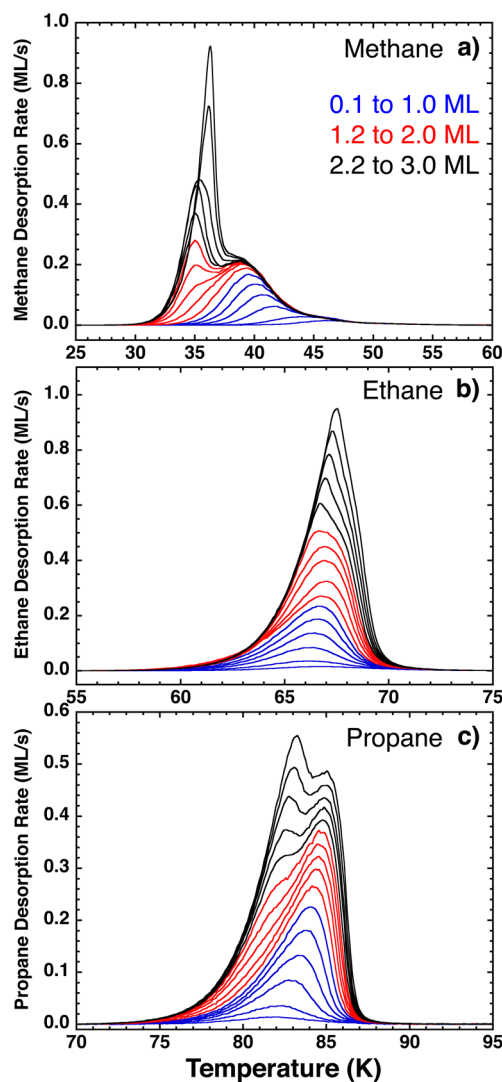


**Figure 7.** TPD spectra for (a) methane, (b) ethane, and (c) propane on ASW for coverages from 0.1 to 1.0 ML (blue curves), 1.2 to 2.0 ML (red curves), and 2.2 to 3.0 ML (black curves). All adsorbates were deposited at 25 K and heated at 1.0 K/s.

and the equation is rearranged to give the coverage dependent desorption energy,  $E_{\text{des}}(\theta) = -RT \ln((-d\theta/dt)/\nu\theta^n)$ . This equation is solved using an experimental TPD spectrum, a value of  $n = 1$  (first order desorption for the results here) and an assumed constant prefactor,  $\nu$ . This results in an  $E_{\text{des}}(\theta)$  curve that is then used to numerically integrate the Polanyi–Wigner equation to generate a set of TPD spectra with coverages less than the inverted TPD. The difference between the simulated and the experimental TPD set (chi square error) is calculated. The process is repeated using a new value for the prefactor until the value that best fits the experimental data is determined.

The procedure is illustrated using the desorption of methane from ASW as an example. Figure 8a displays the  $E_{\text{des}}(\theta)$  curves obtained by inverting the 2 ML TPD for methane in (see inset Figure 8a) with prefactors of  $10^{13}$ ,  $10^{14}$ ,  $10^{15}$ ,  $10^{16}$ , and  $10^{17} \text{ s}^{-1}$ . For an individual curve, the value of  $E_{\text{des}}(\theta)$  increases slightly from 2 ML to  $\sim 1.2$  ML. Near  $\sim 1.2$  ML there is a small inflection (step) in  $E_{\text{des}}(\theta)$ , which then continues to gradually increase until a coverage of  $\sim 0.1$  ML, whereupon it increases sharply. The sharp increase at low coverages (0.1 ML) is due to the presence of relatively high energy binding sites. These sites

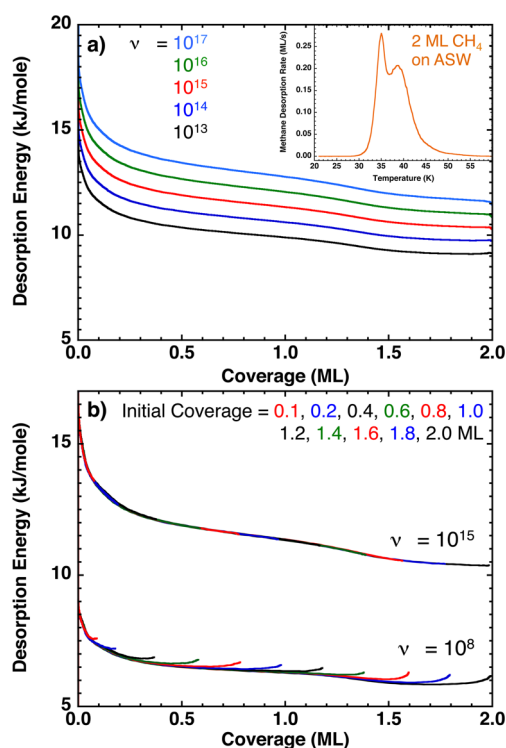


**Figure 8.** (a) Coverage dependent desorption energy curves,  $E_{\text{des}}(\theta)$ , obtained by inverting the 2 ML TPD spectrum of methane on ASW using prefactors,  $\nu$ , of  $10^{13}$  (black curve),  $10^{14}$  (blue curve),  $10^{15}$  (red curve),  $10^{16}$  (green curve), and  $10^{17}$  s $^{-1}$  (light blue curve). (Inset) The 2 ML methane TPD spectrum used for the inversion procedure. (b) Coverage dependent desorption energy curves obtained by inverting methane TPD spectra with initial coverages from 0.1 to 2.0 ML and using  $E_{\text{des}}(\theta)$  curves obtained with prefactors of  $10^{15}$  s $^{-1}$  (upper set of curves) and  $10^8$  s $^{-1}$  (lower set of curves).

are analogous to defect sites on metal or metal oxide single crystal surfaces. The overall pattern is the same for all five curves except that desorption energy is shifted to a higher value with increasing value of the prefactor.

It can be instructive to invert the lower coverage (<2 ML) TPD spectra. Although this not necessary for the inversion procedure it can be useful to narrow the range of potential prefactors. Figure 8b displays the  $E_{\text{des}}(\theta)$  curves obtained from methane TPD spectra with initial coverages from 0.1 to 2.0 ML using prefactors of  $10^8$  s $^{-1}$  and  $10^{15}$  s $^{-1}$ . The  $E_{\text{des}}(\theta)$  curves obtained with a prefactor of  $10^{15}$  s $^{-1}$  are perfectly aligned onto a single curve whereas the curves obtained with a prefactor of  $10^8$  s $^{-1}$  do not align and instead veer upward at higher coverages. The alignment of all of the inverted TPD spectra onto a single curve is consistent with the desorption energy being dependent only on the coverage at the time of desorption. That is, the desorption energy does not also depend on the initial dose. This has to be the case for the desorption energy to be a single valued function of the coverage,  $E_{\text{des}}(\theta)$  and thus, these results suggest that the “best” prefactor will be closer to  $10^{15}$  s $^{-1}$  than to  $10^8$  s $^{-1}$ . Prefactors greater than  $10^{15}$  s $^{-1}$  yield curves that exhibit downward curvature near the initial coverage (not shown).

The next step in the inversion process is to use the  $E_{\text{des}}(\theta)$  curves in Figure 8a to simulate the experimental TPD. Figure 9a displays the simulated methane TPD spectra for an initial coverage of 0.6 ML (solid lines) using the  $E_{\text{des}}(\theta)$  curves obtained using prefactors of  $10^{13}$ ,  $10^{15}$ , and  $10^{17}$  s $^{-1}$ . Also

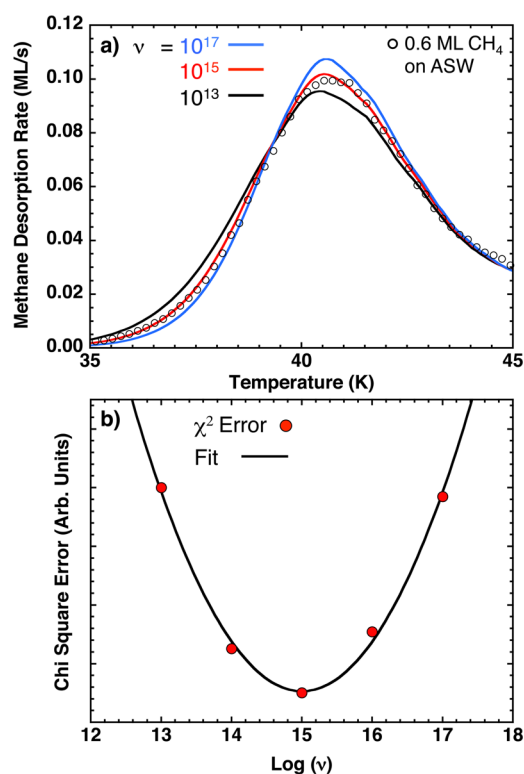


**Figure 9.** (a) Simulated TPD spectra for an initial coverage of 0.6 ML of methane on ASW using the  $E_{\text{des}}(\theta)$  curves in Figure 7a for prefactors of  $10^{13}$  (black curve),  $10^{15}$  (red curve), and  $10^{17}$  s $^{-1}$  (blue curve). Also plotted is the experimental TPD spectrum for 0.6 ML of methane on ASW from Figure 6a (open circles). (b) The total chi square error (solid circles) between the experimental and simulated TPD spectra for all initial coverages vs the log of the prefactor used in the inversion analysis. The solid line is a quadratic fit to the chi square error points and yields a minimum at a value of 14.99 ( $\nu = 9.8 \times 10^{14}$  s $^{-1}$ ).

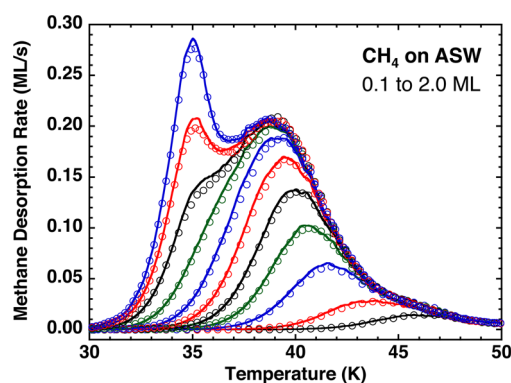


**Figure 10.** Comparison of experimental (open circles) and simulated (lines) TPD spectra for initial methane coverages of 0.1, 0.2, 0.4, 0.6, 0.8, 1.0, 1.2, 1.4, 1.6, 1.8, and 2.0 ML on ASW. The simulated spectra were obtained using the  $E_{\text{des}}(\theta)$  curve obtained with a prefactor of  $\nu = 9.8 \times 10^{14}$  s $^{-1}$ .

plotted is the experimental TPD spectrum for 0.6 ML methane (open circles). Among the three simulations, the simulation with a prefactor of  $10^{15}$  s $^{-1}$  appears to be the best fit to the experiment. Simulations with other initial coverages were also simulated (not shown). The difference between all of the experimental and simulated was used to calculate the total chi square error for each prefactor. Figure 9b displays the chi

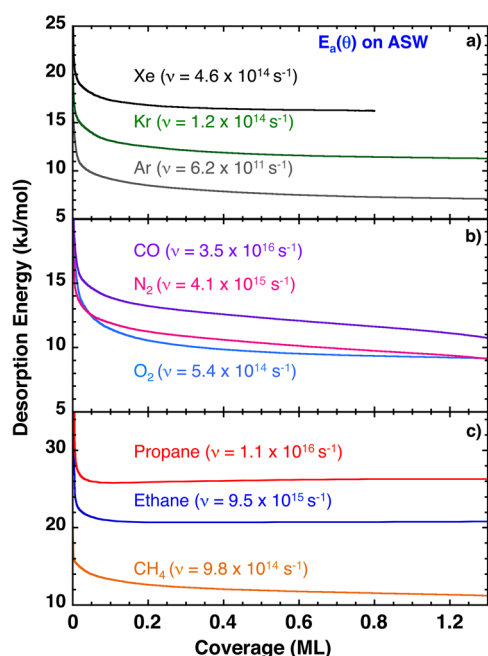


**Figure 11.** Plot of the  $E_{\text{des}}(\theta)$  curves on ASW vs coverage for (a) Xe, Kr, and Ar, (b)  $\text{O}_2$ ,  $\text{N}_2$ , and CO, and (c) methane, ethane, and propane. Also shown are the prefactors used in the inversion analysis to obtain the respective  $E_{\text{des}}(\theta)$  curves.

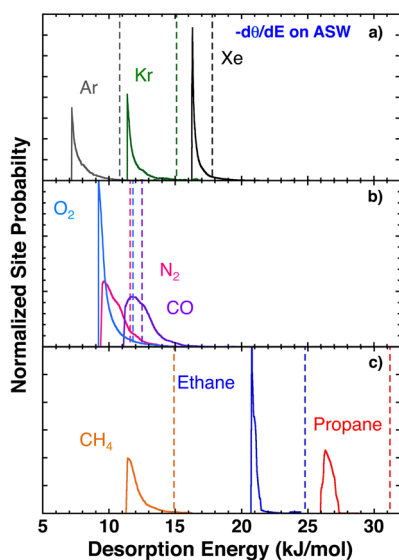


**Figure 12.** Normalized site probability,  $P(E) = -d\theta/dE$ , vs desorption energy on ASW for (a) Xe, Kr, and Ar, (b)  $\text{O}_2$ ,  $\text{N}_2$ , and CO, and (c) methane, ethane, and propane. The vertical dashed lines mark the monolayer adsorbate binding energies on graphene given in Table 1.

square total error (solid circles) obtained from simulations with various prefactors. The solid line is a quadratic fit that has a minimum at a value of 14.99 ( $\nu = 9.8 \times 10^{14} \text{ s}^{-1}$ ). A comparison of the experimental TPD (open circles) and the simulated spectra (solid lines) obtained with a prefactor of  $9.8 \times 10^{14} \text{ s}^{-1}$  and the corresponding  $E_{\text{des}}(\theta)$  curve are displayed in Figure 10. The agreement between the experiment and simulations is excellent. We estimate the error for the  $E_{\text{des}}(\theta)$  curve to be  $\sim \pm 5\%$  and for  $\nu$  to be  $\sim 10^{\pm 0.5}$ .

The inversion procedure was repeated for all of the adsorbates. The highest coverage TPD curve before alignment

**Table 2.** Comparison of Monolayer Binding Energies on Graphene and ASW

adsorbate	graphene (Table 1; kJ/mol)	ASW (most probable; Figure 12; kJ/mol)
argon (Ar)	10.8	7.2
krypton (Kr)	15.1	11.4
xenon (Xe)	17.8	16.3
nitrogen ( $\text{N}_2$ )	11.6	9.6
carbon monoxide (CO)	12.5	11.8
oxygen ( $\text{O}_2$ )	11.8	9.2
methane ( $\text{CH}_4$ )	14.9	11.4
ethane ( $\text{C}_2\text{H}_6$ )	24.8	20.7
propane ( $\text{C}_3\text{H}_8$ )	31.2	26.3

of the leading edges was used to generate the  $E_{\text{des}}(\theta)$  curve for each adsorbate. Figure 11 displays the  $E_{\text{des}}(\theta)$  curves calculated with the “best” fit prefactors for all of the adsorbates. The atomic adsorbates (Ar, Kr, and Xe) are plotted in Figure 11a, the diatomic species ( $\text{O}_2$ ,  $\text{N}_2$ , and CO) are plotted in Figure 11b, and the molecular species (methane, ethane, and propane) are plotted in Figure 11c. In all cases there is a gradual increase in the  $E_{\text{des}}(\theta)$  with decreasing coverage until the coverage is below  $\sim 0.05$  ML, where it increases more steeply. Note that for ethane and propane the increase in  $E_{\text{des}}(\theta)$  from 1.3 to 0.05 ML is very small, which suggests a narrow distribution of binding site energies.

The distribution of binding site energies,  $P(E)$ , can be calculated by differentiating the  $E_{\text{des}}(\theta)$  curves in Figure 11,  $P(E) = -d\theta/dE$ . The calculated,  $P(E)$  distributions for all of the adsorbates on ASW are displayed in Figure 12. The vertical dashed lines mark the monolayer adsorbate binding energies on graphene given in Table 1. The atomic species, Ar, Kr, and Xe (Figure 12a), all have  $P(E)$  curves that are sharply peaked with a tail that extends to higher energy. The  $P(E)$  curves for the diatomic species,  $\text{O}_2$ ,  $\text{N}_2$ , and CO (Figure 12b), are somewhat broader and less peaked. The  $P(E)$  curves for ethane and propane (Figure 12c) are sharply peaked which is consistent with the very flat  $E_{\text{des}}(\theta)$  curves in Figure 11c. The methane  $P(E)$  curve is more reminiscent of that observed for the atomic species. The observation that the  $E_{\text{des}}(\theta)$  curves for the larger hydrocarbons (ethane and propane) are relatively flat, while for methane the curve is more coverage-dependent, may be related to the heterogeneity length scale on the ASW surface. For the larger molecules, the surface interaction is averaged over a larger area and the desorption energy loses its coverage dependence. For methane, the surface interaction area is smaller and a stronger coverage dependence is observed. This suggests that the heterogeneity length scale on ASW is less than the lateral spacing of ethane but larger than that of methane. A more quantitative estimate would require more detailed experiments and analysis. For all of the adsorbates, the peak of the  $P(E)$  curve is at a lower energy than the binding energy on graphene (vertical dashed lines). A summary of the monolayer desorption energies on graphene and the most probable desorption energies on ASW (peak of the  $P(E)$  curve) is given in Table 2.

#### IV. DISCUSSION AND CONCLUSIONS

The experimental results clearly show that, for the nine adsorbates studied here, desorption from a graphene covered Pt(111) substrate occurs with zero-order desorption kinetics.

This is the case for both submonolayer and multilayer coverages. The well-resolved desorption peaks and the alignment of the desorption leading edges are hallmarks of zero-desorption (Figure 3). Zero-order desorption kinetics in the submonolayer coverage regime are indicative of two-phase coexistence between a high-density condensed phase and a low-density gas phase in two dimensions. This two-dimensional, two-phase coexistence arises from attractive adsorbate–adsorbate interactions. The results in the present paper are consistent with our results for methanol, ethanol, and water, which also displayed zero-order desorption kinetics from graphene.<sup>31</sup> Zero-order desorption kinetics have also been reported for desorption from a related carbon surface namely, highly oriented pyrolytic graphite (HOPG).<sup>47</sup> In that work, the desorption kinetics for 23 species were studied and for all of the adsorbates that were also studied by us (CO, N<sub>2</sub>, O<sub>2</sub>, Xe in the present paper and ethanol and methanol in ref 31.) zero-order desorption kinetics were observed. An Arrhenius analysis was used to obtain the binding energies for all of the adsorbates and these values are summarized in Table 1. Also note that the desorption energies determined on the HPOG substrate<sup>47</sup> are in excellent agreement with those determined here and in ref 31. This provides strong evidence that the adsorbate interactions on the two substrates (HOPG and graphene covered Pt) are the same. A table comparing the desorption activation energies obtained on a graphene covered Pt substrate with those obtained on a highly oriented pyrolytic graphite (HOPG) substrate is provided in the Supporting Information.

The desorption kinetics from ASW are markedly different than those from graphene. For example, alignment of the desorption leading edges on a single curve was not observed for any of the nine adsorbates for coverages up to 2 ML. Also, none adsorbates had clearly resolved first and second layer desorption features. The TPD results suggested that the ASW surface has a distribution of binding site energies. In this case, the coverage dependent binding energies were determined using an inversion analysis procedure (Figure 11). The energy distributions for adsorbates of the same type (atomic, diatomic, molecular) have similar shapes and widths (Figure 12). The monolayer TPD peaks on ASW occur at markedly lower temperatures than they do on graphene. This clearly indicates that the interaction of the adsorbates with ASW is noticeably weaker than their interaction with graphene. A comparison of the monolayer desorption energy on graphene and the most probable desorption energy on ASW (see Table 2) shows that the monolayer adsorbate binding energy is greater on graphene than on ASW.

These results show the desorption kinetics from these two astrophysically important substrates need to be analyzed differently. The specific desorption order and mechanism are required to extract adsorbate binding energies needed for accurate models of evaporation from interstellar and planetary ices. Future work will focus on how adsorbate coadsorption affects the desorption kinetics.

## ■ ASSOCIATED CONTENT

### ■ Supporting Information

The Supporting Information is available free of charge on the ACS Publications website at DOI: 10.1021/acs.jpcc.5b10033.

A table comparing the desorption activation energies obtained on a graphene covered Pt substrate with those

obtained on a highly oriented pyrolytic graphite (HOPG) substrate is provided (PDF).

## ■ AUTHOR INFORMATION

### Corresponding Authors

\*Phone: (509) 371-6156. E-mail: scott.smith@pnnl.gov.

\*Phone: (509) 371-6143. E-mail: bruce.kay@pnnl.gov.

### Notes

The authors declare no competing financial interest.

## ■ ACKNOWLEDGMENTS

This work was supported by the U.S. Department of Energy (DOE), Office of Science, Office of Basic Energy Sciences, Division of Chemical Sciences, Geosciences, and Biosciences. The research was performed using EMSL, a national scientific user facility sponsored by DOE's Office of Biological and Environmental Research and located at Pacific Northwest National Laboratory, which is operated by Battelle for the DOE under Contract No. DE-AC05-76RL01830.

## ■ REFERENCES

- (1) Sandford, S. A.; Allamandola, L. J. The Condensation and Vaporization Behavior of Ices Containing SO<sub>2</sub>, H<sub>2</sub>S, and CO<sub>2</sub> - Implications for Io. *Icarus* **1993**, *106*, 478–488.
- (2) Sandford, S. A.; Allamandola, L. J. Condensation and Vaporization Studies of CH<sub>3</sub>OH and NH<sub>3</sub> Ices - Major Implications for Astrochemistry. *Astrophys. J.* **1993**, *417*, 815–825.
- (3) Fraser, H. J.; Collings, M. P.; McCoustra, M. R. S.; Williams, D. A. Thermal Desorption of Water Ice in the Interstellar Medium. *Mon. Not. R. Astron. Soc.* **2001**, *327*, 1165–1172.
- (4) Collings, M. P.; Anderson, M. A.; Chen, R.; Dever, J. W.; Viti, S.; Williams, D. A.; McCoustra, M. R. S. A Laboratory Survey of the Thermal Desorption of Astrophysically Relevant Molecules. *Mon. Not. R. Astron. Soc.* **2004**, *354*, 1133–1140.
- (5) Viti, S.; Collings, M. P.; Dever, J. W.; McCoustra, M. R. S.; Williams, D. A. Evaporation of Ices near Massive Stars: Models Based on Laboratory Temperature Programmed Desorption Data. *Mon. Not. R. Astron. Soc.* **2004**, *354*, 1141–1145.
- (6) Brown, W. A.; Bolina, A. S. Fundamental Data on the Desorption of Pure Interstellar Ices. *Mon. Not. R. Astron. Soc.* **2007**, *374*, 1006–1014.
- (7) Williams, D. A.; Brown, W. A.; Price, S. D.; Rawlings, J. M. C.; Viti, S. Molecules, Ices and Astronomy. *Astron. Geophys.* **2007**, *48*, 25–34.
- (8) Thrower, J. D.; Burke, D. J.; Collings, M. P.; Dawes, A.; Holtom, P. D.; Jamme, F.; Kendall, P.; Brown, W. A.; Clark, I. P.; Fraser, H. J.; McCoustra, M. R. S.; Mason, N. J.; Parker, A. W. Desorption of Hot Molecules from Photon Irradiated Interstellar Ices. *Astrophys. J.* **2008**, *673*, 1233–1239.
- (9) Burke, D. J.; Brown, W. A. Ice in Space: Surface Science Investigations of the Thermal Desorption of Model Interstellar Ices on Dust Grain Analogue Surfaces. *Phys. Chem. Chem. Phys.* **2010**, *12*, 5947–5969.
- (10) Katz, N.; Furman, I.; Biham, O.; Pirronello, V.; Vidali, G. Molecular Hydrogen Formation on Astrophysically Relevant Surfaces. *Astrophys. J.* **1999**, *522*, 305–312.
- (11) Pirronello, V.; Liu, C.; Roser, J. E.; Vidali, G. Measurements of Molecular Hydrogen Formation on Carbonaceous Grains. *Astron. Astrophys.* **1999**, *344*, 681–686.
- (12) Perry, J. S. A.; Price, S. D. Detection of Rovibrationally Excited H<sub>2</sub> Formed through the Heterogeneous Recombination of H Atoms on a Cold Hopg Surface. *Astrophys. Space Sci.* **2003**, *285*, 769–776.
- (13) Sack, N. J.; Baragiola, R. A. Sublimation of Vapor-Deposited Water Ice Below 170-K, and Its Dependence on Growth-Conditions. *Phys. Rev. B: Condens. Matter Mater. Phys.* **1993**, *48*, 9973–9978.

- (14) Smith, R. S.; Huang, C.; Wong, E. K. L.; Kay, B. D. The Molecular Volcano: Abrupt  $\text{CCl}_4$  Desorption Driven by the Crystallization of Amorphous Solid Water. *Phys. Rev. Lett.* **1997**, *79*, 909–912.
- (15) Westley, M. S.; Baratta, G. A.; Baragiola, R. A. Density and Index of Refraction of Water Ice Films Vapor Deposited at Low Temperatures. *J. Chem. Phys.* **1998**, *108*, 3321–3326.
- (16) Stevenson, K. P.; Kimmel, G. A.; Dohnalek, Z.; Smith, R. S.; Kay, B. D. Controlling the Morphology of Amorphous Solid Water. *Science* **1999**, *283*, 1505–1507.
- (17) Ayotte, P.; Smith, R. S.; Stevenson, K. P.; Dohnalek, Z.; Kimmel, G. A.; Kay, B. D. Effect of Porosity on the Adsorption, Desorption, Trapping, and Release of Volatile Gases by Amorphous Solid Water. *J. Geophys. Res.* **2001**, *106*, 33387–33392.
- (18) Kimmel, G. A.; Dohnalek, Z.; Stevenson, K. P.; Smith, R. S.; Kay, B. D. *J. Chem. Phys.* **2001**, *114*, 5295–5303.
- (19) Kimmel, G. A.; Stevenson, K. P.; Dohnalek, Z.; Smith, R. S.; Kay, B. D. Control of Amorphous Solid Water Morphology Using Molecular Beams. I. Experimental Results. *J. Chem. Phys.* **2001**, *114*, 5284–5294.
- (20) Baragiola, R. A. Water Ice on Outer Solar System Surfaces: Basic Properties and Radiation Effects. *Planet. Space Sci.* **2003**, *51*, 953–961.
- (21) Dohnalek, Z.; Kimmel, G. A.; Ayotte, P.; Smith, R. S.; Kay, B. D. *J. Chem. Phys.* **2003**, *118*, 364–372.
- (22) Raut, U.; Fama, M.; Teolis, B. D.; Baragiola, R. A. Characterization of Porosity in Vapor-Deposited Amorphous Solid Water from Methane Adsorption. *J. Chem. Phys.* **2007**, *127*, 204713.
- (23) Zubkov, T.; Smith, R. S.; Engstrom, T. R.; Kay, B. D. Adsorption, Desorption, and Diffusion of Nitrogen in a Model Nanoporous Material. I. Surface Limited Desorption Kinetics in Amorphous Solid Water. *J. Chem. Phys.* **2007**, *127*, 184707.
- (24) Zubkov, T.; Smith, R. S.; Engstrom, T. R.; Kay, B. D. Adsorption, Desorption, and Diffusion of Nitrogen in a Model Nanoporous Material. II. Diffusion Limited Kinetics in Amorphous Solid Water. *J. Chem. Phys.* **2007**, *127*, 184708.
- (25) Smith, R. S.; Zubkov, T.; Dohnalek, Z.; Kay, B. D. The Effect of the Incident Collision Energy on the Porosity of Vapor-Deposited Amorphous Solid Water Films. *J. Phys. Chem. B* **2009**, *113*, 4000–4007.
- (26) May, R. A.; Smith, R. S.; Kay, B. D. Probing the Interaction of Amorphous Solid Water on a Hydrophobic Surface: Dewetting and Crystallization Kinetics of Asw on Carbon Tetrachloride. *Phys. Chem. Chem. Phys.* **2011**, *13*, 19848–19855.
- (27) Smith, R. S.; Matthiesen, J.; Knox, J.; Kay, B. D. Crystallization Kinetics and Excess Free Energy of  $\text{H}_2\text{O}$  and  $\text{D}_2\text{O}$  Nanoscale Films of Amorphous Solid Water. *J. Phys. Chem. A* **2011**, *115*, 5908–5917.
- (28) Smith, R. S.; Petrik, N. G.; Kimmel, G. A.; Kay, B. D. Thermal and Nonthermal Physicochemical Processes in Nanoscale Films of Amorphous Solid Water. *Acc. Chem. Res.* **2012**, *45*, 33–42.
- (29) May, R. A.; Smith, R. S.; Kay, B. D. The Release of Trapped Gases from Amorphous Solid Water Films. I. “Top-Down” Crystallization-Induced Crack Propagation Probed Using the Molecular Volcano. *J. Chem. Phys.* **2013**, *138*, 104501.
- (30) May, R. A.; Smith, R. S.; Kay, B. D. The Release of Trapped Gases from Amorphous Solid Water Films. II. “Bottom-up” Induced Desorption Pathways. *J. Chem. Phys.* **2013**, *138*, 104502.
- (31) Smith, R. S.; Matthiesen, J.; Kay, B. D. Desorption Kinetics of Methanol, Ethanol, and Water from Graphene. *J. Phys. Chem. A* **2014**, *118*, 8242–8250.
- (32) Bolina, A. S.; Wolff, A. J.; Brown, W. A. Reflection Absorption Infrared Spectroscopy and Temperature-Programmed Desorption Studies of the Adsorption and Desorption of Amorphous and Crystalline Water on a Graphite Surface. *J. Phys. Chem. B* **2005**, *109*, 16836–16845.
- (33) Bolina, A. S.; Wolff, A. J.; Brown, W. A. Reflection Absorption Infrared Spectroscopy and Temperature Programmed Desorption Investigations of the Interaction of Methanol with a Graphite Surface. *J. Chem. Phys.* **2005**, *122*, 044713.
- (34) Burke, D. J.; Wolff, A. J.; Edridge, J. L.; Brown, W. A. The Adsorption and Desorption of Ethanol Ices from a Model Grain Surface. *J. Chem. Phys.* **2008**, *128*, 104702.
- (35) Smith, R. S.; Zubkov, T.; Kay, B. D. The Effect of the Incident Collision Energy on the Phase and Crystallization Kinetics of Vapor Deposited Water Films. *J. Chem. Phys.* **2006**, *124*, 114710.
- (36) Tait, S. L.; Dohnalek, Z.; Campbell, C. T.; Kay, B. D. N-Alkanes on Pt(111) and on C(0001)/Pt(111): Chain Length Dependence of Kinetic Desorption Parameters. *J. Chem. Phys.* **2006**, *125*, 234308.
- (37) Kimmel, G. A.; Matthiesen, J.; Baer, M.; Mundy, C. J.; Petrik, N. G.; Smith, R. S.; Dohnalek, Z.; Kay, B. D. No Confinement Needed: Observation of a Metastable Hydrophobic Wetting Two-Layer Ice on Graphene. *J. Am. Chem. Soc.* **2009**, *131*, 12838–12844.
- (38) Daschbach, J. L.; Peden, B. M.; Smith, R. S.; Kay, B. D. Adsorption, Desorption, and Clustering of  $\text{H}_2\text{O}$  on Pt(111). *J. Chem. Phys.* **2004**, *120*, 1516–1523.
- (39) Kimmel, G. A.; Persson, M.; Dohnalek, Z.; Kay, B. D. Temperature Independent Physisorption Kinetics and Adsorbate Layer Compression for Ar Adsorbed on Pt(111). *J. Chem. Phys.* **2003**, *119*, 6776–6783.
- (40) Linstrom, P. J.; Mallard, W. G. *NIST Chemistry Webbook, NIST Standard Reference Database Number 69*; National Institute of Standards and Technology: Gaithersburg, MD; <http://webbook.nist.gov>, Accessed on September 18th, 2015.
- (41) *CRC Handbook of Chemistry and Physics: 1993–1994: A Ready-Reference Book of Chemical and Physical Data*; Lide, D. R., Ed.; CRC Press: Boca Raton, FL, 1993.
- (42) Tait, S. L.; Dohnalek, Z.; Campbell, C. T.; Kay, B. D. N-Alkanes on MgO(100). I. Coverage-Dependent Desorption Kinetics of N-Butane. *J. Chem. Phys.* **2005**, *122*, 164707.
- (43) Tait, S. L.; Dohnalek, Z.; Campbell, C. T.; Kay, B. D. N-Alkanes on MgO(100). II. Chain Length Dependence of Kinetic Desorption Parameters for Small N-Alkanes. *J. Chem. Phys.* **2005**, *122*, 164708.
- (44) Dohnalek, Z.; Kim, J.; Bondarchuk, O.; White, J. M.; Kay, B. D. Physisorption of  $\text{N}_2$ ,  $\text{O}_2$ , and CO on Fully Oxidized  $\text{TiO}_2(110)$ . *J. Phys. Chem. B* **2006**, *110*, 6229–6235.
- (45) Smith, R. S.; Li, Z. J.; Chen, L.; Dohnalek, Z.; Kay, B. D. Adsorption, Desorption, and Displacement Kinetics of  $\text{H}_2\text{O}$  and  $\text{CO}_2$  on  $\text{TiO}_2(110)$ . *J. Phys. Chem. B* **2014**, *118*, 8054–8061.
- (46) Smith, R. S.; Li, Z. J.; Dohnalek, Z.; Kay, B. D. Adsorption, Desorption, and Displacement Kinetics of  $\text{H}_2\text{O}$  and  $\text{CO}_2$  on Forsterite,  $\text{Mg}_2\text{SiO}_4(011)$ . *J. Phys. Chem. C* **2014**, *118*, 29091–29100.
- (47) Ulbricht, H.; Zacharia, R.; Cindir, N.; Hertel, T. Thermal Desorption of Gases and Solvents from Graphite and Carbon Nanotube Surfaces. *Carbon* **2006**, *44*, 2931–2942.